Slow light in mass-produced, dispersion-engineered photonic crystal ring resonators

KATHLEEN MCGARVEY-LECHABLE,[1] TABASSOM HAMIDFAR,[1] DAVID PATEL,[2] LUHUA XU,[2] DAVID V. PLANT,[2] AND PABLO BIANUCCI[1,*]

[1]*Department of Physics, Concordia University, Montreal, Quebec, H4B 1R6 Canada*
[2]*Department of Electrical and Computer Engineering, McGill University, Montreal, Quebec, H3A 2A7, Canada*
[*]*pablo.bianucci@concordia.ca*

Abstract: We present experimental results of photonic crystal ring resonators (PhCRRs) fabricated on the CMOS-compatible, silicon-on-insulator platform via 193-nm deep-UV lithography. Our dispersion-engineering design approach is compared to experimental results, showing very good agreement between theory and measurements. Specifically, we report a mean photonic band-edge wavelength of 1546.2 ± 5.8 nm, a 0.2% variation from our targeted band-edge wavelength of 1550 nm. Methods for the direct calculation of the experimental, discrete dispersion relation and extraction of intrinsic quality factors for a highly-dispersive resonator are discussed. A maximum intrinsic quality factor of ≈83,800 is reported, substantiating our design method and indicating that high-throughput optical lithography is a viable candidate for PhCRR fabrication. Finally, through comparison of the mean intrinsic quality and slowdown factors of the PhCRRs and standard ring resonators, we present evidence of an increase in light-matter interaction strength with simultaneous preservation of microcavity lifetimes.

OCIS codes: (350.4238) Nanophotonics and photonic crystals; (230.5750) Resonators.

References and links

1. B. Little, S. Chu, H. Haus, J. Foresi, and J.-P. Laine, "Microring resonator channel dropping filters," J. Lightwave Technol. **15**, 998–1005 (1997).
2. V. R. Almeida, C. A. Barrios, R. R. Panepucci, and M. Lipson, "All-optical control of light on a silicon chip," Nature **431**, 1081–4 (2004).
3. M. Ferrera, D. Duchesne, L. Razzari, M. Peccianti, R. Morandotti, P. Cheben, S. Janz, D.-X. Xu, B. E. Little, S. Chu, and D. J. Moss, "Low power four wave mixing in an integrated, micro-ring resonator with Q = 12 million," Opt. Express **17**, 14098 (2009).
4. Y. Liu, Y. Xuan, X. Xue, P.-H. Wang, S. Chen, A. J. Metcalf, J. Wang, D. E. Leaird, M. Qi, and A. M. Weiner, "Investigation of mode coupling in normal-dispersion silicon nitride microresonators for Kerr frequency comb generation," Optica **1**, 137 (2014).
5. V. Brasch, M. Geiselmann, T. Herr, G. Lihachev, M. H. P. Pfeiffer, M. L. Gorodetsky, and T. J. Kippenberg, "Photonic chip-based optical frequency comb using soliton Cherenkov radiation," Science **351**, 357 LP – 360 (2016).
6. C. Reimer, M. Kues, P. Roztocki, B. Wetzel, F. Grazioso, B. E. Little, S. T. Chu, T. Johnston, Y. Bromberg, L. Caspani, D. J. Moss, and R. Morandotti, "Generation of multiphoton entangled quantum states by means of integrated frequency combs," Science (New York, N.Y.) **351**, 1176–80 (2016).
7. I.S. Grudinin and N. Yu, "Dispersion engineering of crystalline resonators via microstructuring," Optica **3**, 221–224 (2015).
8. K. Y. Yang, K. Beha, D. Cole, X. Yi, P. Del'Haye, H. Lee, J. Li, D. Oh, S. A. Diddams, S .B. Papp, and K.J. Vahala, "Broadband dispersion-engineered microresonator on a chip," Nat. Photon. **10**, 316-320 (2016).
9. K. Saha, Y. Okawachi, J. S. Levy, and R. K. W. Lau, K. Luke, M. A. Foster, M. Lipson, and A. L. Gaeta, "Broadband parametric frequency comb generation with a 1-μm pump source," Opt. Express **20**, 26935–26941 (2012).
10. M. S. McClellan, L. L. Domier, and R. C. Bailey, "Label-free virus detection using silicon photonic microring resonators," Biosens. Bioelectron. **31**, 388–92 (2012).
11. M. Sumetsky, R. S. Windeler, Y. Dulashko, and X. Fan, "Optical liquid ring resonator sensor," Opt. Express **15**, 14376 (2007).
12. C. E. Campanella, F. De Leonardis, L. Mastronardi, P. Malara, G. Gagliardi, and V. M. N. Passaro, "Investigation of refractive index sensing based on Fano resonance in fiber Bragg grating ring resonators," Opt. Express **23**, 14301–13 (2015).

13. D. Goldring, U. Levy, and D. Mendlovic, "Highly dispersive micro-ring resonator based on one dimensional photonic crystal waveguide design and analysis," Opt. Express **15**, 3156 (2007).
14. K. McGarvey-Lechable and P. Bianucci, "Maximizing slow-light enhancement in one-dimensional photonic crystal ring resonators," Opt. Express **22**, 26032 (2014).
15. L. Thévenaz, I. Dicaire, and S. Chin, "Enhancing the light-matter interaction using slow light: towards the concept of dense light," in "SPIE OPTO," S. M. Shahriar and F. A. Narducci, eds. (International Society for Optics and Photonics, 2012), pp. 82731D–82731D–8.
16. M. Soljacić, E. Lidorikis, L. V. Hau, and J. D. Joannopoulos, "Enhancement of microcavity lifetimes using highly dispersive materials," Phys. Rev. E Stat. Nonlin. Soft Matter Phys. **71**, 026602 (2005).
17. J. Y. Lee and P. M. Fauchet, "Slow-light dispersion in periodically patterned silicon microring resonators," Opt. Lett. **37**, 58–60 (2012).
18. G. Gao, Y. Zhang, H. Zhang, Y. Wang, Q. Huang, and J. Xia, "Air-mode photonic crystal ring resonator on silicon-on-insulator," Sci. Rep. **6**, 19999 (2016).
19. M. Settle, M. Salib, A. Michaeli, and T. F. Krauss, "Low loss silicon on insulator photonic crystal waveguides made by 193nm optical lithography," Opt. Express **14**, 2440 (2006).
20. S. Johnson and J. Joannopoulos, "Block-iterative frequency-domain methods for Maxwell's equations in a planewave basis," Opt. Express **8**, 173 (2001).
21. A. Y. Petrov and M. Eich, "Zero dispersion at small group velocities in photonic crystal waveguides," Appl. Phys. Lett. **85**, 4866 (2004).
22. E. Kuramochi, M. Notomi, S. Hughes, A. Shinya, T. Watanabe, and L. Ramunno, "Disorder-induced scattering loss of line-defect waveguides in photonic crystal slabs," Phys. Rev. B **72**, 161318 (2005).
23. T. F. Krauss, "Slow light in photonic crystal waveguides," J. Phys. D: Appl. Phys. **40**, 2666–2670 (2007).
24. D. Urbonas, A. Balčytis, K. Vaškevičius, M. Gabalis, and R. Petruškevičius, "Air and dielectric bands photonic crystal microringresonator for refractive index sensing," Opt. Lett. **41**, 3655–3658 (2016).

1. Introduction

An essential characteristic of an integrated photonic circuit is the ability to regulate the flow of light. One component of a photonic circuit which has proven particularly successful in this regard is the microscale ring resonator (RR). A low-loss RR possesses sharp spectral features, resulting in strong mode confinement which can be useful for narrow-band optical filters [1] and switches [2]. In addition, the high-intensity, localized electromagnetic fields of a RR's mode can lead to strong interactions between the fields and the constituent material of the resonator, allowing for the observation of optical non-linear effects such as four-wave mixing [3], frequency comb generation [4, 5] and quantum-entangled photon states [6]. Additionally, ring resonators can be dispersion-engineered through variations of the underlying waveguide dispersion so as to enhance the performance of non-linear devices [7–9]. In recent years, RRs have also shown considerable promise as sensitive detection systems for biological and chemical analytes [10–12].

A photonic crystal ring resonator (PhCRR) stands to improve upon the optical features of a RR. A PhCRR is a hybrid device consisting of a standard RR with an overlying photonic crystal (PhC) structure. (see Fig. 1(a)) [13]. The PhCRR provides augmented control of the propagation of light waves by utilizing the slow-light effects of its PhC lattice. Due to the periodic nature of the PhC waveguide's dielectric material, the dispersion relation exhibits non-linear behaviour near the photonic band edge (PBE). Through careful selection of design parameters [14], PhCRR's can be engineered to possess resonances exhibiting slow-light characteristics such as enhanced light-matter interactions [15] and improved microcavity lifetimes [16]. The strong dispersion of a ring's photonic crystal lattice can also be used to further refine control over existing dispersion-engineering techniques.

Silicon photonics has emerged at the forefront of integrated photonics technologies due to its CMOS-compatible manufacturing processes. The silicon-on-insulator (SOI) platform capitalizes on the high refractive index contrast between its oxide substrate and silicon top layer that allows for miniaturization of photonic features up to the sub-micron scale. Previous PhCRRs have been fabricated on the SOI platform using electron-beam lithography; Lee et. al [17] first demonstrated non-uniform mode spacing indicative of slow-light wave propagation in fabricated photonic crystal ring resonators with a maximum reported Q-factor of $Q \sim 2000$ and group

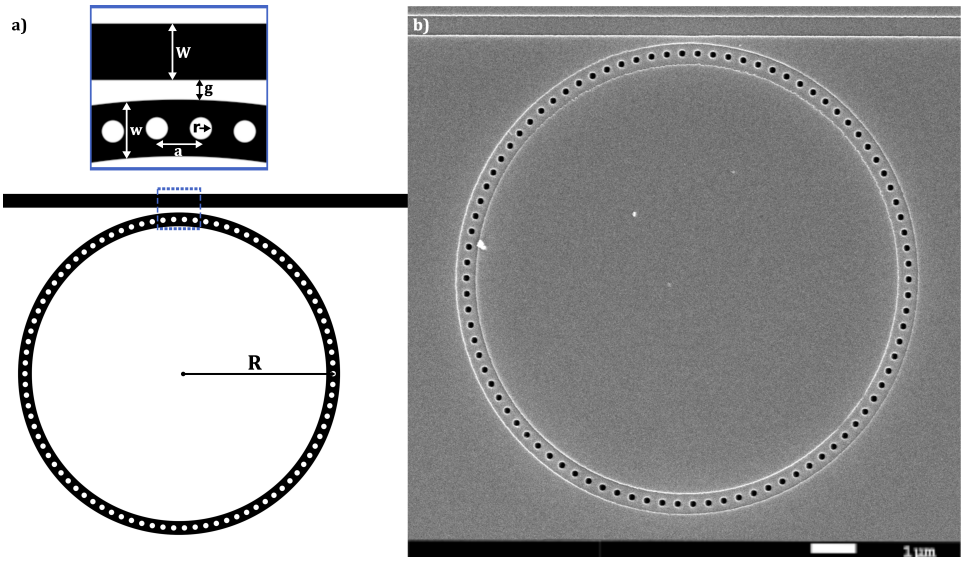

Fig. 1. (a) The geometry of a PhCRR. The high refractive index material is indicated in black and the low-index, background material is indicated in white. (b) A scanning electron microscope image of a 10-μm-diameter PhCRR evanescently coupled to a 0.450 μm wide strip waveguide.

index of $n_g \sim 20$, while Gao et al. [18] successfully decreased optical losses by nearly an order of magnitude, with a maximum reported Q-factor of $Q \sim 14{,}800$ and group index of $n_g \sim 28$. Accordingly, the high fabrication resolution of electron-beam lithography has been proven acceptable for fabricating the nanoscale features of a PhCRR. However, its low throughput and costly fabrication methods render the technology unsuitable for mass manufacturing of integrated photonic circuits. Alternatively, optical lithography technologies are relatively low-cost and allow for straightforward upscaling of fabrication processes. In particular, 193-nm deep-UV lithography has demonstrated comparable fabrication tolerances to those of electron-beam lithography [19].

In this work, the experimental results of on-chip, dispersion-engineered PhCRRs fabricated via the CMOS-compatible, 193-nm deep-UV lithography process (ePIXfab IMEC Standard Passives) are presented. A maximum intrinsic quality factor of $8.38x10^4$ is reported, exceeding the PhCRR quality factors reported in devices fabricated via electron-beam lithography and laying the foundation for an on-chip, mass produced, slow light photonic circuit. We demonstrate the high accuracy of our dispersion engineering design approach used for the selection of the PhCRRs' geometric parameters by showing a mean PBE wavelength within 0.2% of our targeted wavelength. In addition, through comparison of the spectra of standard RRs and PhCRRs, we directly demonstrate a photonic band gap in a fabricated PhCRR. As a result of our rigorous mode identification, we are able to introduce for the first time a method for determining the experimental dispersion relation and group indices of a PhCRR and show good agreement between experimental and computational results. In comparison, previous work lacked access to the underlying waveguide dispersion of the PhCRR. Finally, through examination of the slowdown factors and mean intrinsic quality factors of fabricated PhCRRs and their equivalently-sized RRs, we present evidence of an increase in light-matter interaction strength with simultaneous preservation of microcavity lifetimes.

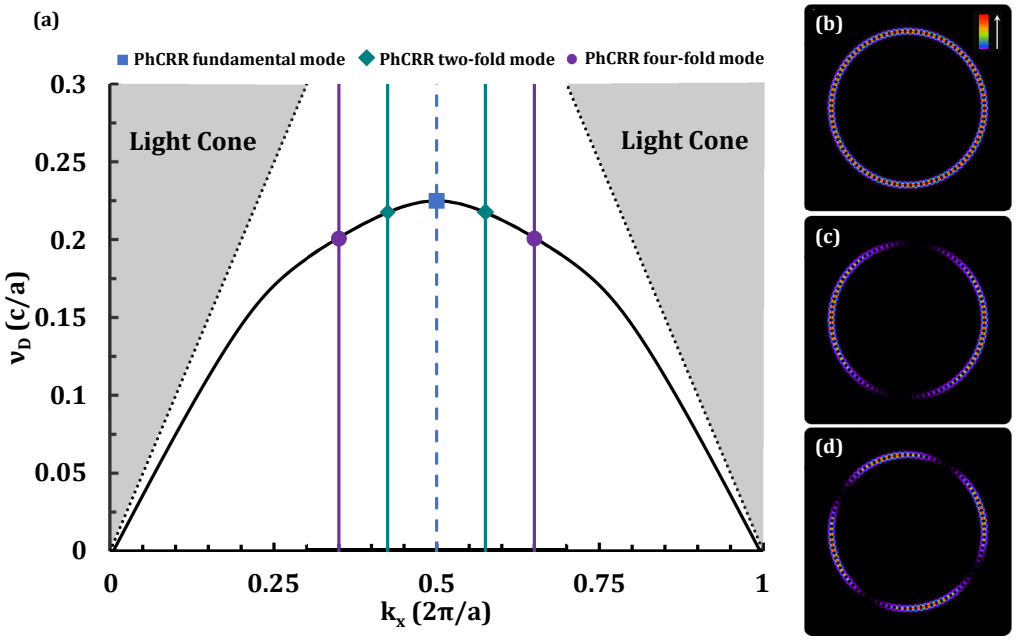

Fig. 2. (a) The dispersion relation of the first photonic band of an infinitely-long SOI PhC waveguide of width $w = 1.3a$, and $f = 0.243$. The photonic band edge is denoted as the dotted vertical line. (b,c,d) The electric field energy densities of the fundamental, two-fold, and four-fold PhCRR modes, respectively.

2. Design and computational results

The geometric parameters for the on-chip PhCRRs are selected using the design prescription described in [14]. Firstly, the dispersion relation of a silicon PhC strip waveguide ($n_{Si} = 3.18$) on a 2.0-μm-thick silica substrate ($n_{SiO_2} = 1.44$) is simulated in 3-dimensions using the frequency-domain MIT Photonic Bands (MPB) software package [20]. The PhC waveguide is considered to be infinitely long with a width of $w = 1.3a$ and a height of $t = 220$ nm, where a is defined as the lattice period of the PhC. The infinite PhC waveguide's continuous range of frequency eigenvalues are discretized by mapping the waveguide onto a spatially-bound RR structure. This is achieved by imposing boundary conditions ensuring periodicity of the PhC lattice and phase-matching of the PhCRR's resonances. Finally, an iterative approach is used to scale the PBE dimensionless frequency, v_D, of the PhC waveguide's dielectric photonic band to the target wavelength, $\lambda_0 = 1550$ nm (corresponding to the transparency window of silicon), by varying the filling factor of the PhC lattice and recalculting the dispersion relation as needed. The resulting geometric parameters selected for the PhCRRs are lattice period $a = 348$ nm, waveguide width $w = 1.3a = 452$ nm, PhC hole radius $r = 85$ nm, and filling factor $f = \frac{r}{a} = 0.243$ (see Fig. 1(b)).

Figure 2(a) displays the dispersion relation of the infinitely long PhC waveguide computed with MPB. The periodic boundary conditions are graphically represented by the vertical lines. The resonances of the PhCRR are found where the vertical lines intersect with the PhC waveguide's dispersion relation. The fundamental (i.e. band-edge) mode, corresponding to mode number $\frac{N}{2}$, where N represents the number of PhC lattice periods, is found directly at the PBE (denoted here as the vertical dotted line). The two-fold and four-fold modes, corresponding to mode numbers $m = (\frac{N}{2}) \pm 1$ and $m = (\frac{N}{2}) \pm 2$ respectively, both possess frequency degeneracies due to the symmetry of the dispersion relation about the PBE. 2D FDTD simulations provide qualitative analysis of the PhCRR's resonant field configurations. As is seen in Figs. 2(b), (c), and (d),

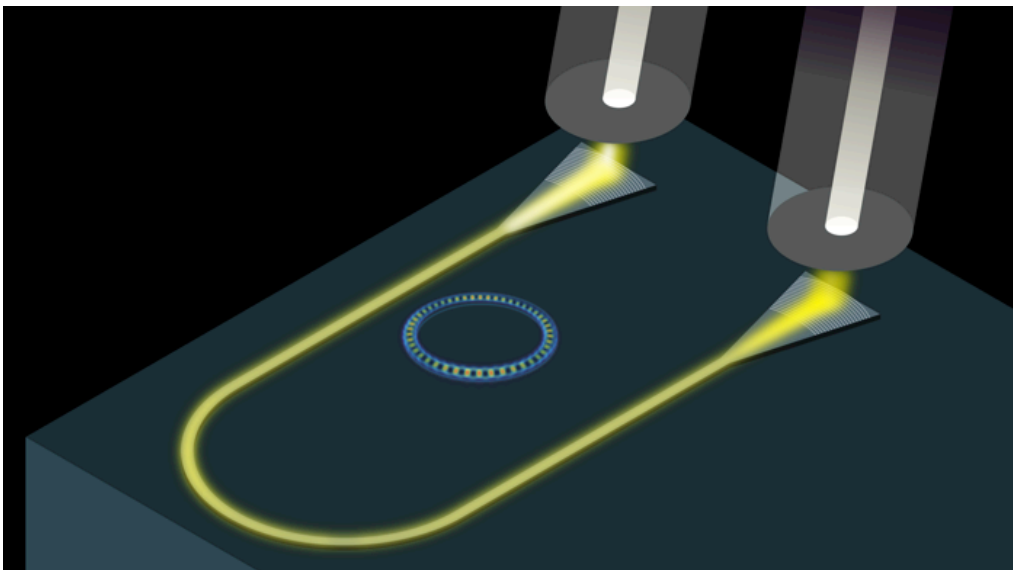

Fig. 3. The experimental setup utilized for the characterization of the devices. Each PhCRR is evanescently coupled to an input waveguide and the transmission spectrum is monitored via an output waveguide coupled to an optical fiber (figure not to scale).

the electric fields are highly concentrated in the material of the PhCRR, confirming that the resonances can be found on the “dielectric" band of the PhC waveguide. This attribute makes PhCRRs particularly suitable for the observation of non-linear optical phenomena. It is worth noting that the above design method can easily be generalized so as to target resonances on the “air" band of the PhC waveguide, where the strength of the field is concentrated in the air holes of the PhC lattice [18]. This particular field configuration may prove interesting for biological or chemical sensors, where strong light-matter interactions can enhance the detection of analytes. Interference patterns of the electric field energy densities due to the linear combination of frequency-degenerate, counter propagating modes are also observed in the two-fold and four-fold configurations.

3. Fabrication and characterization

Thirty PhCRRs are fabricated on a SOI wafer consisting of a 220-nm-thick silicon top layer on a 2-μm-thick silica layer. When designing the PhCRRs for fabrication via optical lithography processes, design biases must be added to the dimensions of the resist mask to ensure the fabricated dimensions of the PhCRR’s features are on target. Accordingly, the drawn dimensions of the mask are $w = 462$ nm, $r = 120$ nm, and $f = 0.345$. The PhC lattice is fully etched into the top silicon layer and the devices sit atop the buried oxide silica layer. A top air cladding is utilized to maximize the refractive index contrast of the materials. In order to probe the limit of miniaturization of on-chip PhCRRs, rings of radius equal to 4.985 μm and 10.081 μm (corresponding to lattice periods N equal to 90 and 182, respectively) are fabricated. Standard ring resonators of equivalent size are also placed on the chip for comparative purposes. TE-like polarized light from a tunable laser is introduced into the devices via a grating coupler optimized for operation at 1550 nm with a 30 nm bandwidth. Each grating coupler is joined to a strip waveguide of width $W = 450$ nm and the PhCRR is placed a distance of $g = 150$ nm from the strip waveguide to ensure evanescent-field coupling. While simulations show a smaller evanescent gap will produce more efficient coupling between the PhCRR and waveguide, design restrictions

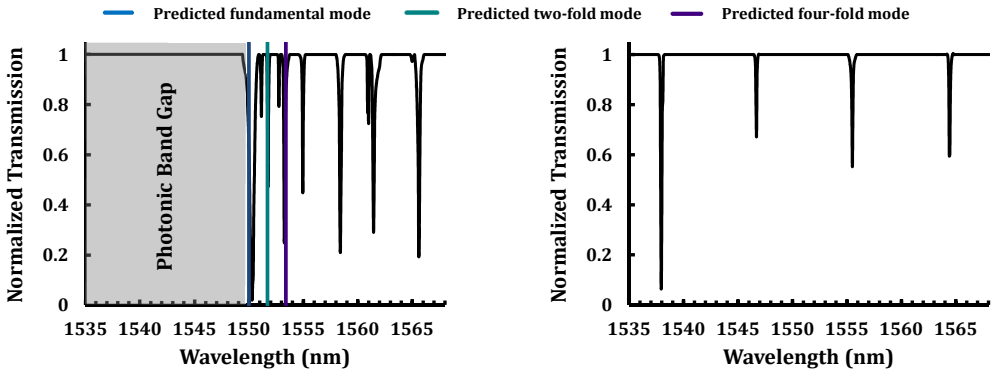

Fig. 4. The spectra of a 20-μm-diameter PhCRR (left) and an equivalently sized standard ring resonator (right). The photonic band gap of the PhCRR is indicated by the shaded region. The wavelengths of the fundamental, two-fold, and four-fold modes of the PhCRR predicted using the design prescription discussed in [14] are indicated by the blue, green, and purple lines, respectively.

of the deep-UV optical lithography process limit the gap to 150 nm. A second grating coupler is found at the end of the strip waveguide to couple the output signal to a power meter that monitors the PhCRR's transmission spectrum (see Fig. 3).

4. Experimental results

The mean fundamental mode of the thirty measured PhCRRs is 1546.2 ± 5.8 nm, a variation of 0.2% from the target wavelength of 1550 nm. This deviation can be attributed to an insufficiency of data concerning the correct design biases to be added to the resist mask of the PhC hole lattice. As a result, it is difficult to ensure that the on-chip filling factor of the PhC lattice will exactly coincide with the design filling factor of $f = 0.243$. Any divergence of the filling factor occurring during a fabrication run will result in a modified dispersion relation and an associated shift in resonances. The design biases of future fabrications of PhCRRs on the deep-UV lithography platform can be adjusted based on comparison of design biases and on-chip hole sizes of the current run to ensure a closer correspondence to the selected target wavelength.

To illustrate the characteristic spectral features of a PhCRR, Fig. 4 compares the measured spectrum of a 20-μm-diameter PhCRR (left) to that of an equivalently sized standard RR (right). The fundamental mode of this particular PhCRR is found precisely at 1550 nm. The PhCRR clearly exhibits a photonic band gap, with no resonances observed below the fundamental mode. In addition, the free spectral range (FSR) between adjacent modes of the PhCRR is non-uniform, increasing with increased distance from the PBE. This non-uniformity can be attributed to the strong dispersion of the PhC lattice near the PBE. Mode splitting due to fabrication-induced surface roughness breaking the frequency-degeneracy of modes found away from the PBE can also be observed. Alternatively, the standard RR displays no photonic band gap and possesses equidistant spacing between adjacent modes.

4.1. Experimental determination of the PhC dispersion relation

The experimentally-determined dispersion relation of a 10-μm-diameter PhCRR is compared to data computed via 2D MPB simulations in Fig. 5(a). To calculate the discrete dispersion relation of the PhCRR, the device is considered as a straight PhC waveguide [14]. Note that the straight waveguide approximation utilized here is valid seeing that the radius of curvature of the 10-μm-

diameter ring is much greater than the optical wavelengths in question (i.e. $R >> \frac{\lambda_0}{n_{eff}}$). The mode number of each transmission dip is determined using the equation $m = \frac{N}{2} \pm p$, where p is an integer quantifying the separation of a mode from the PBE mode (e.g. the fundamental mode has $p = 0$, the two-fold mode has $p = \pm 1$, etc.). As the TE-like electromagnetic wave is propagating through a sub-micron-thick layer of silicon, the field can be considered as a transverse-electric plane wave with wavevector $\mathbf{k} = k_x$. The boundary condition ensuring phase matching of the propagating waves allows the wave vector to be expressed as $k_x = \frac{m}{R}$. The dimensionless frequency of each dip is calculated using the relation $\nu_D = \frac{a}{\lambda_0}$, where λ_0 represents the centre wavelength in free space of each transmission dip [14]. As can be seen in Fig. 5, the experimental dispersion relation is noticeably non-linear, in close agreement with computational results. This non-linearity accounts for the non-uniformity of the PhCRRs' free spectral range and confirms the strong dispersion of the PhCRR near the PBE due to its periodic dielectric structure.

The experimental group indices of the PhCRR are calculated using the relation $n_g = c\frac{dk_x}{d\nu_D}$. The experimental group indices are again in close relation with computation results. At the PBE, the group index is $n_g \approx 23.4$, nearly an order of magnitude greater than the group index of silicon RR modes. Away from the PBE, the group index of the two-fold mode is noticeably higher than was predicted in simulations. This may be due in part to fabrication-induced splitting of frequency degenerate modes. If the width of the splitting is comparable to the FSR of adjacent modes, anti-mode-crossings may occur that result in flat-band regions of the dispersion relation away from the PBE [21]. This interaction between the split resonances of the PhCRR may provide yet another dispersion-engineering method for microresonators, one which provides a much higher degree of control over the over the group indices of engineered regions of the dispersion relation.

4.2. Calculation of intrinsic quality factors

Because light is introduced into the optical resonators via a coupling waveguide, it is necessary to decompose the total quality factor of each device into its constituent contributions. The optical losses can be attributed either to losses due to outcoupling through the waveguide or to intrinsic propagation losses due to nonuniformities of the resonator (e.g. sidewall roughness, disparate PhC hole size, etc.). The two contributions are related to the total quality factor as:

$$\frac{1}{Q_{total}} = \frac{1}{Q_C} + \frac{1}{Q_I} \tag{1}$$

where Q_C and Q_I quantify the coupling and intrinsic quality factors, respectively.

The resonant modes of the linear transmission spectrum of an all-pass ring resonator can be fit using the equation:

$$1 - |T|^2 = \frac{(a^2 - 1)(r^2 - 1)}{1 + r^2a^2 - 2ar\cos(\varphi)} \tag{2}$$

where φ is the phase shift experienced by the fields upon a single round trip of the resonator and $0 < a, r < 1$ are the single-trip attenuation of the electromagnetic fields in the resonator and the fraction of the field transmitted directly through the waveguide, respectively. The phase shift undergone by the fields in a resonator of length L can be expressed as:

$$\varphi = \frac{\omega_0 n_{g_{eff}} L}{c} \tag{3}$$

Here ω_0 is the resonant frequency of a particular mode and $n_{g_{eff}}$ represents the effective group index of a particular resonance. The above variables can be related to the intrinsic and coupling quality factors as:

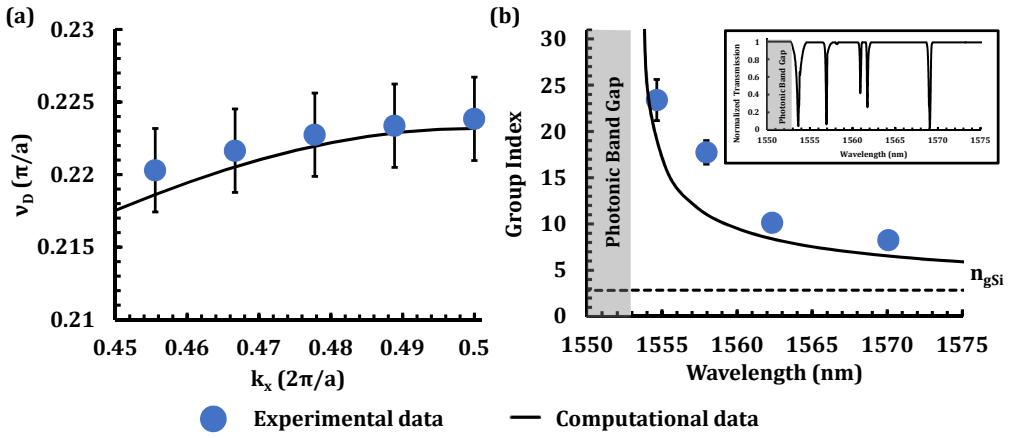

Fig. 5. (a) The experimental dispersion relation of a 10-μm-diameter PhCRR as compared to the simulated dispersion relation of the PhCRR computed via MPB. (b) The experimental group index of a 10-μm-diameter PhCRR as compared to the simulated group relation of the PhCRR computed via MPB. The inset shows the transmission spectrum of the PhCRR in question.

$$Q_C = \frac{\omega_0 \tau_{rt}}{2|\ln(r)|} \qquad Q_I = \frac{\omega_0 \tau_{rt}}{2|\ln(a)|} \tag{4}$$

where τ_{rt} denotes the single-trip time of a photon in the resonator.

While this analysis is valid for a standard RR, it does not account for the strong effects of dispersion in a PhCRR. In order to provide a correction to Eq. (2), we follow the method of [13] and [16] and insert a frequency-dependency into the resonant frequency:

$$\tilde{\omega_0} = \omega_0 \left[1 - \frac{n_{g_{eff}}(\omega) - n_{g_{eff}}(\omega_0)}{n_{g_{eff}}(\omega_0)}\right] \tag{5}$$

By combining Eq. (3) with Eq. (5) and utilizing the phase matching condition of a ring resonator ($\omega_0 \tau_{rt} = 2m\pi$), it is straightforward to find:

$$\varphi(\omega) = \frac{\tau_{rt}\omega_0}{n_{g_{eff}}(\omega_0)}\left[1 - n_{g_{eff}}(\omega)\right] \tag{6}$$

The transmission spectrum of a highly dispersive resonator can thus be described by combining Eqs. (2) and (6). Because the dispersion relation is approximately linear in the close vicinity of each resonant mode, it is sufficient to utilize a linear effective group index, $n_{g_{eff}}(\omega) = b_0 + b_1\omega$ in Eq. (6), where b_0 and b_1 are determined by fitting a linear curve between experimentally determined group indices of adjacent modes.

Using the above method, the intrinsic quality factors of the thirty PhCRRs and thirty equivalently-sized RRs were calculated (see Fig. 6). Because the experimental characterization setup does not allow us to distinguish between r and a, we have assumed that the PhCRRs are undercoupled. We then compare the "worst-case scenario" PhCRR intrinsic Q-factors to the "best-case scenario" RR intrinsic Q-factors. While this method carries the risk of overestimating the PhCRR resonator losses (or, equivalently, underestimating the RR resonator losses), it allows for a conservative comparison of the effect of slow light on a resonator's intrinsic Q-factors.

The PhCRRs were sorted as a function of their mode order (i.e. two-fold and four-fold), so as to more precisely gauge the relation between a mode's quality and slowdown factors (see Fig.

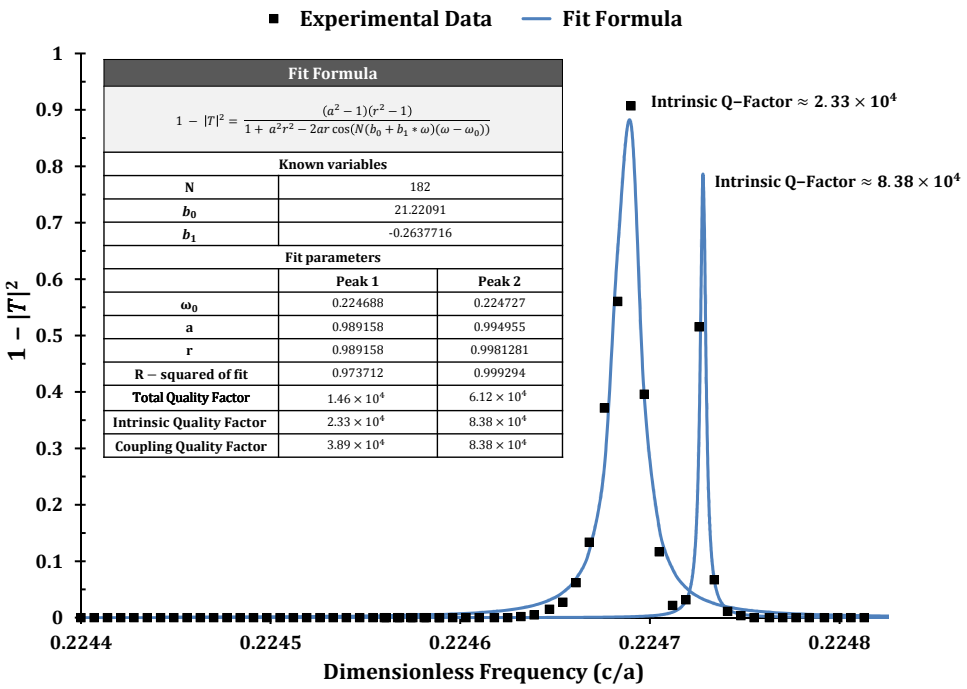

Fit Formula		
$1 - \lvert T\rvert^2 = \frac{(a^2-1)(r^2-1)}{1+a^2r^2-2ar\cos(N(b_0+b_1*\omega)(\omega-\omega_0))}$		
Known variables		
N	182	
b_0	21.22091	
b_1	-0.2637716	
Fit parameters		
	Peak 1	**Peak 2**
ω_0	0.224688	0.224727
a	0.989158	0.994955
r	0.989158	0.9981281
R − squared of fit	0.973712	0.999294
Total Quality Factor	1.46×10^4	6.12×10^4
Intrinsic Quality Factor	2.33×10^4	8.38×10^4
Coupling Quality Factor	3.89×10^4	8.38×10^4

Fig. 6. An example illustrating our peak fitting technique for the split two-fold mode of a 20-μm PhCRR. Each peak was fit using the parameters and known constants detailed in the inset table. The highest intrinsic quality factor of the thirty measured PhCRRs was found at Peak 2.

7). It has been theoretically and experimentally verified that backscattering losses due to the presence of scatterers on the surface of a resonator scales as the square of the group index in the slow light regime [22]. Surface roughness induced losses thus present a substantial hurdle in the design of slow light resonant modes.

As can be seen, the highly dispersive PhC lattice of the PhCRR contributes to an enhancement of slowdown factors by a factor of ≈8. Despite this increase in the effective group index of the devices, however, the intrinsic quality factors of the standard RRs and the PhCRRs are comparable within the measured ranges of the devices. We have thus concluded that our design procedure may be used to place PhCRR resonances in a moderate slow light regime, where the slow light enhancement of resonant modes overcomes optical losses due to the increased group indices. As non-linear effects have been shown to increase quadratically with the slowdown factor [23], this simultaneous enhancement of light-matter interaction strength and preservation of microcavity lifetimes may prove beneficial in the observation of non-linear phenomenon at low powers.

The highest PhCRR intrinsic Q-factor of ≈83,800 was found at the two-fold mode of a 20-μm-diameter PhCRR. To the extent of our knowledge, this is the highest reported quality factor in either the dielectric or air bands of a fabricated PhCRR [17, 18, 24], confirming the validity of our particular design and fabrication methods.

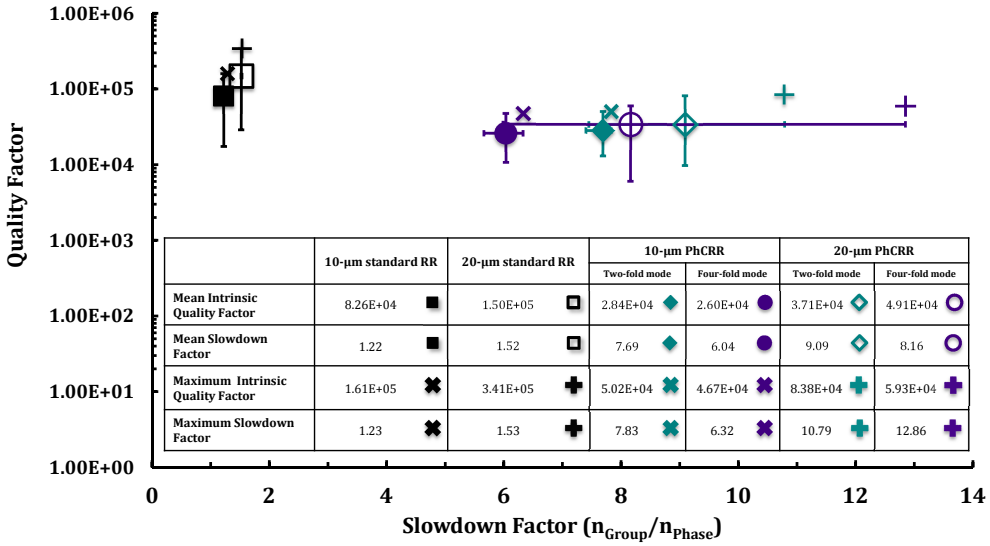

	10-μm standard RR	20-μm standard RR	10-μm PhCRR		20-μm PhCRR	
			Two-fold mode	Four-fold mode	Two-fold mode	Four-fold mode
Mean Intrinsic Quality Factor	8.26E+04	1.50E+05	2.84E+04	2.60E+04	3.71E+04	4.91E+04
Mean Slowdown Factor	1.22	1.52	7.69	6.04	9.09	8.16
Maximum Intrinsic Quality Factor	1.61E+05	3.41E+05	5.02E+04	4.67E+04	8.38E+04	5.93E+04
Maximum Slowdown Factor	1.23	1.53	7.83	6.32	10.79	12.86

Fig. 7. The mean intrinsic quality factors of the 10 μm diameter PhCRRs' two-fold, and four-fold modes as compared to the mean intrinsic quality factors of their equivalently sized standard RRs as a function of the slowdown factor. The vertical and horizontal error bars indicate the range of values of the intrinsic quality factors and slowdown factors, respectively, for the thirty measured devices.

5. Conclusion

In summary, we have presented the experimental results of PhCRRs fabricated on the SOI platform via CMOS-compatible, 193-nm deep-UV lithography. Our mean quality factors for the PhCRRs demonstrate that optical lithography is a preferred platform for PhCRR fabrication as compared to previous work concerning PhCRRs fabricated via e-beam lithography. The spectral features of a standard RR and a PhCRR have been compared, with the latter exhibiting a photonic band gap and strong dispersion at the PBE resulting in non-equidistant spacing between adjacent modes. Due to the high-intensity, localized electric fields found in the dielectric material of the PhCRR and the strong dispersion near the PBE resulting in an enhancement in slowdown factors, we believe that dielectric-band PhCRRs are strong candidates for non-linear devices. These favourable attributes can also be applied to air-band PhCRRs, opening the door for improved detection of biological and chemical analytes. Finally, our maximum reported intrinsic quality factor of ≈83,800, found at the two-fold mode of a 20-μm PhCRR device, leads us to conclude that the slow light enhancement of quality factors overcomes surface-roughness induced losses slightly away from the photonic band edge.

Acknowledgments

We would like to acknowledge CMC Microsystems for the provision of products and services that facilitated this research, including access to the Mentor Graphics software package and fabrication services using the IMEC-ePIXfab SiPhotonics technology. This work was supported by the National Science and Engineering Research Council (NSERC) Discovery grant program and Concordia University.